

Electronic Supplementary Material (ESI) for Catalysis Science & Technology.

Supporting Information

Creation of carbon-defects and in-plane holes with the assistance of NH₄Br to enhance the photocatalytic activity of g-C₃N₄

Guiyang Yu,^{a,b} Haitao Zhao,^c Chuanwang Xing,^d Luyan Guo,^d and Xiyou Li^{*a,d,e}

^a College of Materials Science and Engineering, China University of Petroleum (East China), Qingdao, 266580, China.

^b State Key Laboratory of Inorganic Synthesis and Preparative Chemistry, College of Chemistry, Jilin University, Changchun, 130012, China.

^c Shandong Provincial Key Laboratory of Chemical Energy Storage and Novel Cell Technology, Liaocheng University, Liaocheng 252059, PR China.

^d College of Science, China University of Petroleum (East China), Qingdao, 266580, China

^e State Key Laboratory of Heavy Oil Processing, China University of Petroleum (East China), Qingdao, 266580, China. Email: xiyouli@upc.edu.cn

Content

Experimental Section

Scheme S1. Route of condensation from melamine to melem, directly or via melam, then to the linear polymer melon.

Fig. S1 Br 3d XPS spectrum of NH₄Br and CN-Br-T320 samples.

Fig. S2 Average pore width of CN-Br (1:30) samples.

Fig. S3 AFM images of bulk CN and CN-Br (1:30) samples.

Fig. S4 Nitrogen adsorption-desorption isotherms of CN and CN-Br (1:x, x=10, 30, 40) samples.

Fig. S5 FTIR spectra of CN and CN-Br (1:x, x=10, 30, 40).

Fig. S6 Elemental content of CN and CN-Br samples by (a) ICP analysis and (b) XPS analysis. (c) comparison of composition change based on different analysis method.

Fig. S7 (a) XPS survey spectrum, (b) high-resolution O 1s of bulk CN and CN-Br (1:30) samples.

Fig. S8 The area ratio of various C species upon (a) bulk CN and (b) CN-Br (1:30) samples after fitting.

Fig. S9 Comparison of time-dependent amounts of H₂ generation (a) and H₂ evolution rates (b) over bulk CN and CN-Br samples with 10 vol% triethanolamine (TEOA) aqueous solution, 1.0 % Pt as a cocatalyst and 0.1 g photocatalysts under visible-light irradiation.

Fig. S10 (a) UV-vis absorbance spectra of RhB solution (10 mg·L⁻¹) and CN-Br (1:30) sample. (b) EDS analysis and corresponding TEM image of inset for RhB/CN-Br (1:30)

in H_2PtCl_4 aqueous solution after light irradiation with the wavelength of larger 550 nm. (c) Schematic diagram of hypothesized photosensitization process of RhB and (d) actual result.

Fig. S11 (a) UV-vis absorbance spectra of RhB solution ($10 \text{ mg}\cdot\text{L}^{-1}$). (b) Photocatalytic performance of bulk CN and CN-Br samples in RhB degradation with visible-light irradiation. (c) The apparent rate constant (k) over bulk CN and CN-Br samples in RhB degradation reaction.

Fig. S12 (a) Effect of quencher additives on the photocatalytic activity of CN-Br (1:30) sample in RhB degradation. (b) EPR spectra of bulk CN and CN-Br (1:30) samples with visible-light irradiation for 300s for the detection of $\cdot\text{O}_2^-$ radicals in the presence of DMPO. (c) UV-vis absorbance spectra of NBT solution ($2.5\times 10^{-5}\text{M}$). (d) Quantitative determination of $\cdot\text{O}_2^-$ generation for bulk CN and CN-Br (1:30) samples via time-dependent degradation of NBT solution ($2.5\times 10^{-5}\text{M}$) under visible-light irradiation. (e) Reaction equation between NBT and $\cdot\text{O}_2^-$ is 1:4 in molar ratio.

Fig. S13 UV-vis absorbance spectra of degradation NBT reaction upon (a) bulk CN and (b) CN-Br (1:30) sample.

Fig. S14 (a) XRD patterns, (b) FTIR spectra, (c) C 1s and (d) N 1s XPS spectra of CN-Br (1:30) sample before and after reaction.

Fig. S15 (a) Illustration of charge behavior in holy $\text{g-C}_3\text{N}_4$ with carbon defect upon light illustration. (b) The enhancement of photocatalytic hydrogen evolution and degradation rate based on BET surface area enhancement and the introduction of carbon defects.

Table S1. The atomic content of C and N elements, and the ratio of C to N of CN and CN-Br samples by using XPS and ICP analysis.

Table S2. Composition and chemical properties of CN and CN-Br samples.

Table S3. Normalized degradation efficiency with their BET specific surface areas.

References

Experimental Section

Preparation of photocatalysts:

CN-Br was prepared by a one-step pyrolysis treatment of melamine and ammonium bromide (NH_4Br) mixture. In detail, 1.0 g melamine and a certain amount of NH_4Br were added into 40 mL de-ionized water and kept stirring for 4 hours. Then the mixture was heated at 80 °C in open air to remove water and other volatiles. The dried mixture was calcined in a muffle furnace under static air atmosphere with programmed heating method (the rate of 1.7 °C/min). The heating program has three steps, firstly the sample was heated from room temperature to 320 °C and kept at this temperature for 30 min. Secondly, the sample was continually heated to 450 °C and maintained at this temperature for 30 min. In the last step, the sample was heated to 500 °C and kept at this temperature for two hours. After this reaction process completed, the temperature was naturally cooled to room temperature and the yellow sample was ground in an agent mortar to obtain product powder. Samples prepared with different molar ratios of melamine to NH_4Br (1:10; 1:30 and 1:40) were labelled as CN-Br (1:10), CN-Br (1:30), and CN-Br (1:40), respectively. As comparison, the bulk CN is prepared by directly thermal polymerization of melamine. The sample was heated to 500 °C with the temperature rising rate of 1.7 °C/min, and then kept at this temperature for 2 hours.

Preparation of the intermediates of melamine- NH_4Br mixture:

The intermediates of melamine- NH_4Br mixture were obtained via heating at different temperatures (320 °C, 450 °C and 500 °C) for 2 hours, which was labeled as CN-Br-T320, CN-Br-T450, and CN-Br-T500, respectively.

Characterization:

The crystallite property was examined using the X-ray diffraction (XRD) characterization containing a Rigaku X-ray diffractometer of Cu K α radiation ($\lambda=1.5418$ Å, 50 kV, 200 mA). The scanning rate is 10°/min from 10° to 60°. The thermal decomposition and weight loss of samples were determined using the thermogravimetric (TG) measurement with the NETZSCH STA 449c thermal station

and the heating rate was controlled at 1.7 °C min⁻¹. The morphology and holey property were investigated using JEOL JSM-6700F field-emission scanning electronic microscope (SEM) and JEM 2100 transmission electron microscopy (TEM) with the accelerating voltage of 10 kV and 200 kV, respectively. Fourier transform infrared spectra (FTIR) was performed to determine the change of functional moieties with Bruker V70 spectrometer. Hitachi UV-3900 spectrophotometer was used to analyse the UV-vis diffused reflectance spectra (DRS) of the samples, in which BaSO₄ acts as blank reference. Atomic force microscopy (AFM) study was recorded on Bruker Multimode 8. The surface areas and pore distribution were determined by N₂ adsorption/desorption isotherms and Brunauer-Emmett-Teller (BET) method. The sample was heated to 150 °C maintaining 5 h in order to evacuate any moisture and solvent molecules inner the pore. The element composition and chemical property were examined by X-ray photoelectron spectroscopy (XPS). The excitation source was Thermo Escalab 250 Xi Mg K α of 1254.6 eV and the calibrated process was used C 1s peak at 284.6 eV as standard. The structural differences of carbon element was identified using a Bruker AVANCE III 400 MHz WB solid-state NMR spectrometer at room temperature. The electronic nature and paramagnetic species of samples were measured on a JES-FA200 EPR spectra. The sweeping magnetic field was at room temperature and experimental parameters were microwave frequency at ν F9441.704, center field of 3506.4 G, and 1 mW power, respectively. Steady-state photoluminescence (PL) and time resolved fluorescence spectra were performed on FLS980 (Edinburgh instrument Ltd, England) at room temperature. The surface photovoltage (SPV) spectra was measured at a 532 nm continuous laser as light source with a chopper (SR540, Stanford Research Systems, Inc.). The measurement system consists of a lock-in amplifier (SR830, Stanford Research Systems, Inc.) and a sample chamber.

Photoelectrochemical measurements

The transient photocurrent responses, and electrochemical impedance spectroscopy (EIS) were investigated on a CHI760D electrochemical workstation

(Shanghai Chenhua Instrument Corp., China) in a conventional three-electrode system composed of a Pt sheet counter electrode, a saturated calomel electrode (SCE) as reference electrode and a working electrode. Firstly, the working electrode was fabricated by spin-coating ethanol suspensions onto pre-cleaned FTO glass ($1 \times 1 \text{ cm}^2$) surface. Typically, 5 mg sample was dispersed evenly in 2 mL ethanol with 10 μL Nafion solution, followed by ultrasonic treatment for 1 h to form homogeneous solution. The above solution was dipped (40 μL) and spin-coated ($200 \text{ r}\cdot\text{min}^{-1}$, 10 s) onto the pre-cleaned FTO conductive glass surface, and then dried at room temperature. The above coating process was repeated ten times. Moreover, 0.5 M Na_2SO_4 aqueous solution was used as supporting electrolyte. A 300 W Xe lamp equipped with a 420 nm optical cutoff filter was used as light source. The photo-responsive signals were measured by I-t curves and the electrochemical impedance spectroscopy was tested at a frequency range from 10^5 to 0.01 Hz.

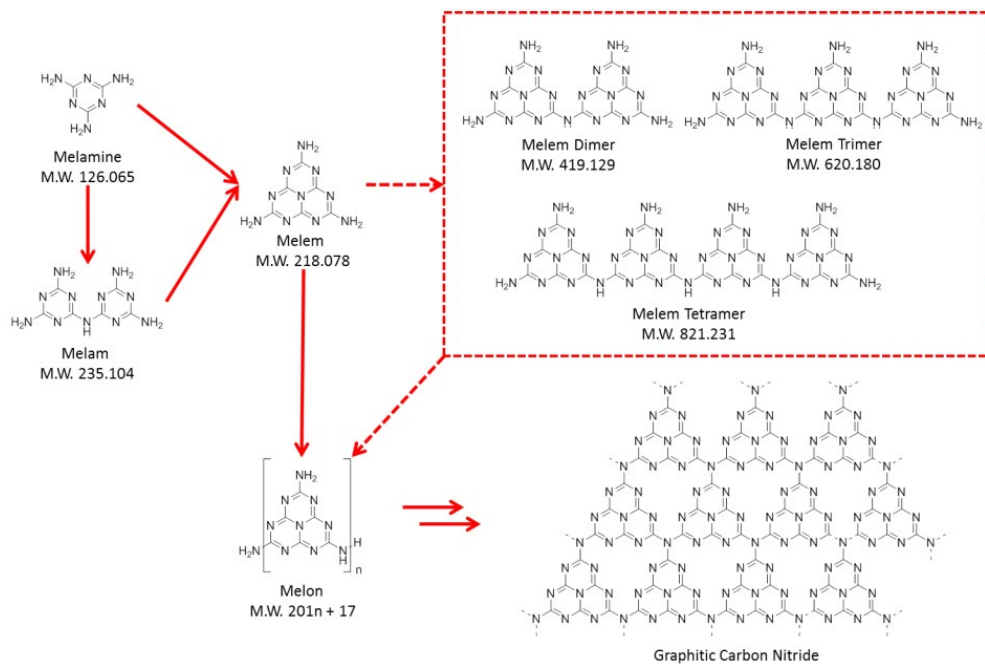
Photocatalytic Reaction Experiment

The photocatalytic H_2 evolution reactions were carried out in a glass close circulation system. 0.1 g photocatalyst was dispersed in 100 mL of aqueous solution containing sacrificial reagent (10 vol% triethanolamine (TEOA)). The reaction temperature was maintained at 5 $^\circ\text{C}$. The system was evacuated 30 min to remove the dissolved air completely prior to light irradiation. Magnetic stirring (300 r/min) was used to keep the photocatalyst particles in a suspension state. A 300 W Xe-lamp (Beijing Perfectlight Technology Co., Ltd. PLS-SXE 300D) with a cutoff filter was employed for irradiation. The area of surface irradiated was about 16.5 cm^2 . The amount of evolved H_2 was determined by an in situ online gas chromatograph (GC7900) equipped with a thermal conductivity detector and a 4 m 5 \AA molecular sieve columns.

Photocatalytic degradation of RhB experiments were measured in a 250 mL quartz vial (Beijing Perfectlight Technology Co., Ltd. QC350) under a top irradiation model. 40 mg photocatalyst powder was dispersed into 80 mL $10 \text{ mg}\cdot\text{L}^{-1}$ RhB solution. This reaction dispersion was magnetically stirring in the dark for 30 min prior to irradiation

to establish the adsorption/desorption equilibrium of the RhB on the catalyst surface. The mixture was then irradiated under a 300 W Xe-lamp with cut-off filter under 5 °C by a cooling water bath. At given irradiation time intervals, 2 mL specimens were taken from the dispersion and centrifuged at 8000 rpm for 10 min to separate the catalyst particles. The concentration of aqueous RhB was determined using UV-vis spectrophotometer at 554 nm by measuring its absorbance. EPR was used to detect radicals spin-trapped by 5,5-dimethyl-1-pyrroline-N-oxide (DMPO) in methanol. The signals were collected by a JES-FA200 with the setting microwave frequency about 9.4417 GHz.

Nitroblue tetrazolium (NBT) degradation reaction was employed to determine the amount of $\cdot\text{O}_2^-$ because NBT can be reduced by $\cdot\text{O}_2^-$ radicals and formed purple formazan, which was insoluble in water. During each photocatalytic reaction, 40 mg photocatalyst was added to a formic acid/water aqueous solution (5 vol%, 80 mL) containing NBT ($2.5 \times 10^{-5} \text{M}$). After continuous stirring for 30 min in dark, 300 W Xe-lamp with cut-off filter was used to irradiate reaction system. Specimens of given time intervals was obtained as same as above operation. The concentration of $\cdot\text{O}_2^-$ radicals was measured by the absorbance change at the wavelength of 260 nm. The molar ratio of generated $\cdot\text{O}_2^-$ radicals and degraded NBT was 4:1, in which the reaction equation was shown in Fig. S12d.



Scheme S1. Route of condensation from melamine to melem, directly or via melam, then to the linear polymer melon. The idealized structure of graphitic carbon nitride is also shown as a hypothesized product of complete melem condensation, as indicated by the double arrow. Scheme adapted from Schwarzer *et al* and Bettina V.

Lotsch

et

al.^{1,2}

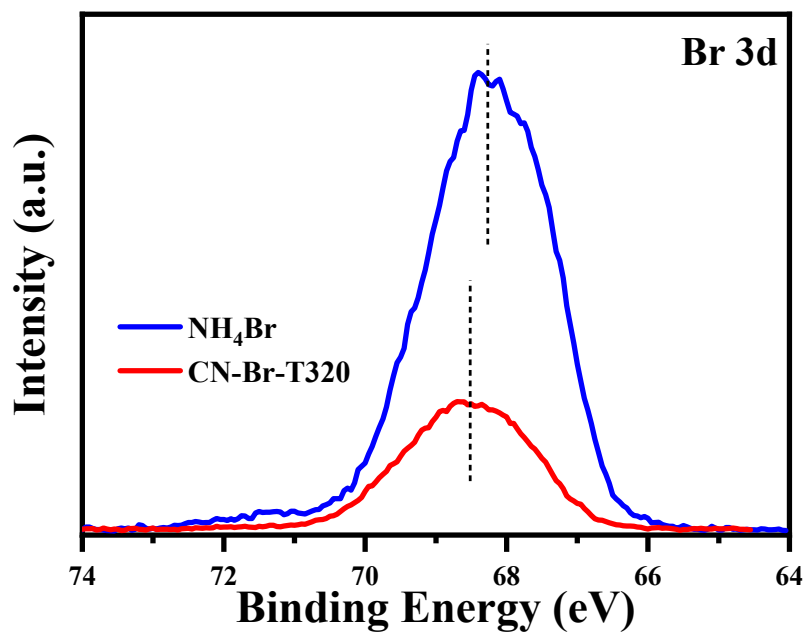


Fig. S1 Br 3d XPS spectrum of NH₄Br and CN-Br-T320 samples.

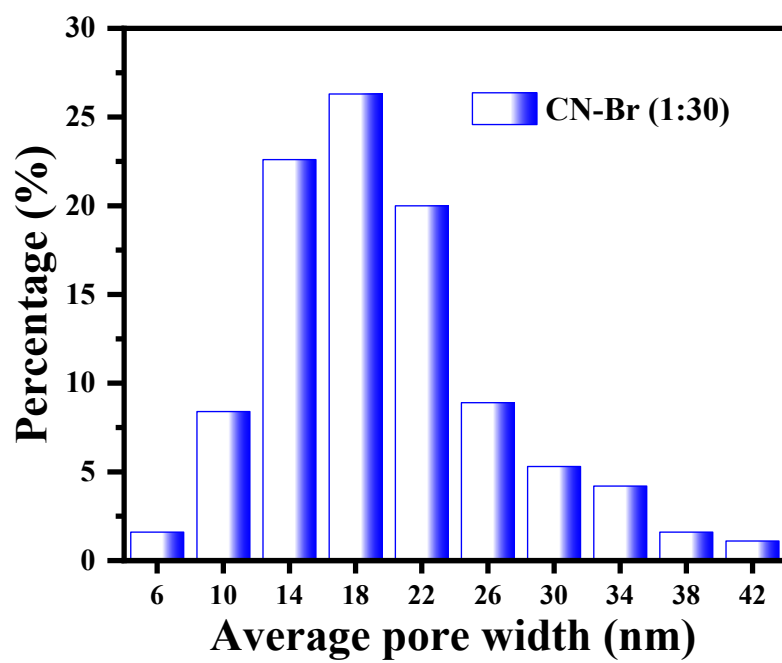


Fig. S2 Average pore width of CN-Br (1:30) samples.

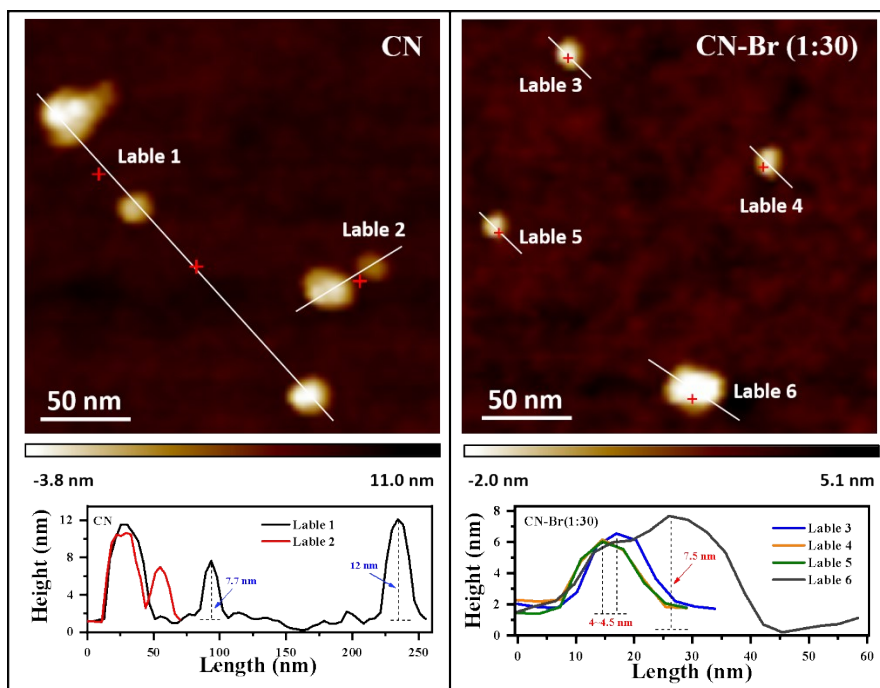


Fig. S3 AFM images of bulk CN and CN-Br (1:30) samples.

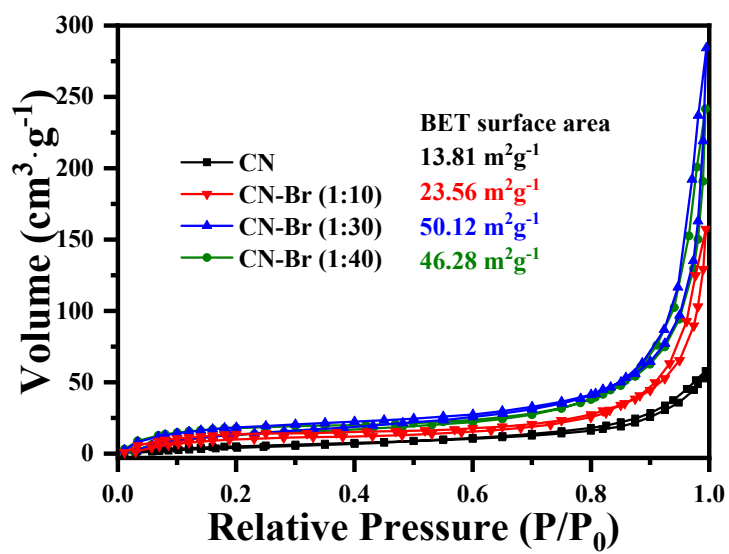


Fig. S4 Nitrogen adsorption-desorption isotherms of CN and CN-Br (1:x, x=10, 30, 40) samples.

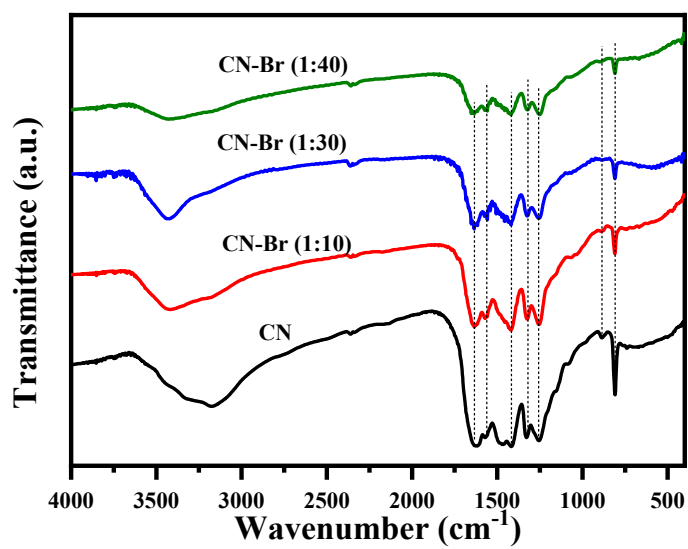


Fig. S5 FTIR spectra of CN and CN-Br (1:x, x=10, 30, 40).

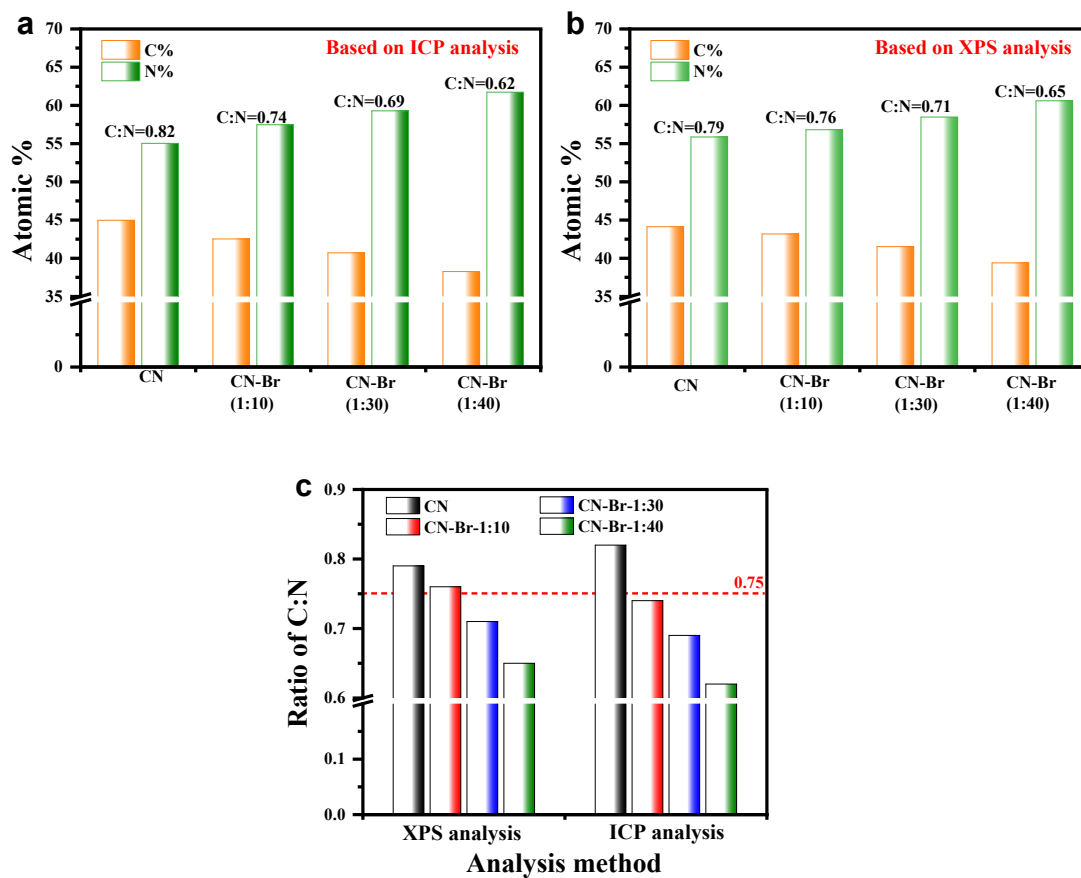


Fig. S6 Elemental content of CN and CN-Br samples by (a) ICP analysis and (b) XPS analysis. (c) comparison of composition change based on different analysis method.

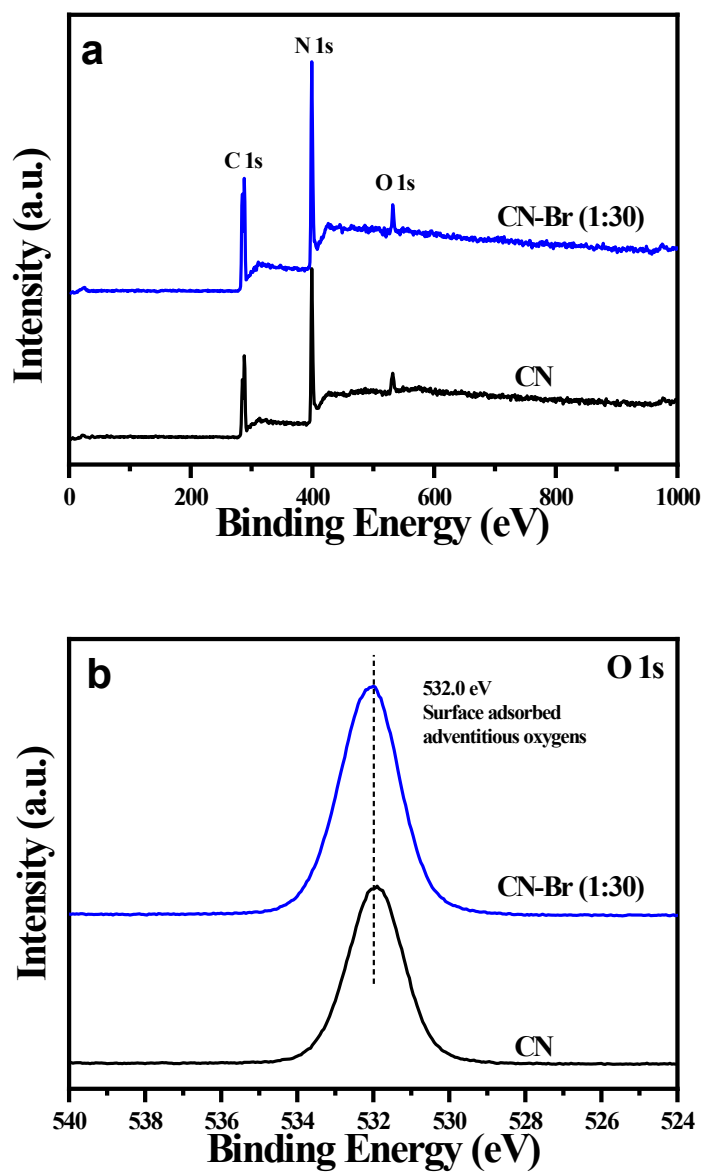


Fig. S7 (a) XPS survey spectrum, (b) high-resolution O 1s of bulk CN and CN-Br (1:30) samples.

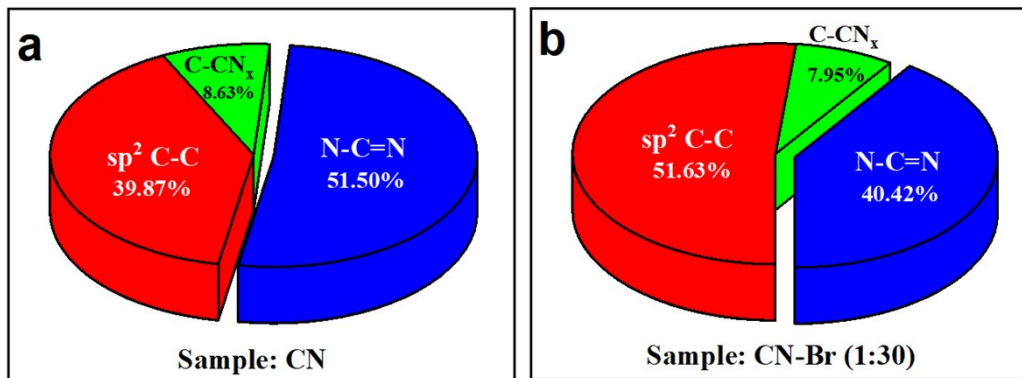


Fig. S8 The area ratio of various C species upon (a) bulk CN and (b) CN-Br (1:30) samples after fitting.

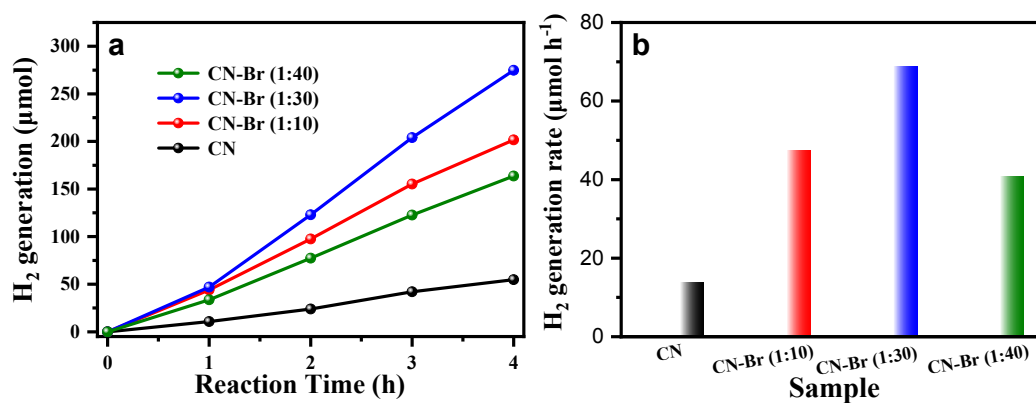


Fig. S9 Comparison of time-dependent amounts of H₂ generation (a) and H₂ evolution rates (b) over bulk CN and CN-Br samples with 10 vol% triethanolamine (TEOA) aqueous solution, 1.0 % Pt as a cocatalyst and 0.1 g photocatalysts under visible-light irradiation.

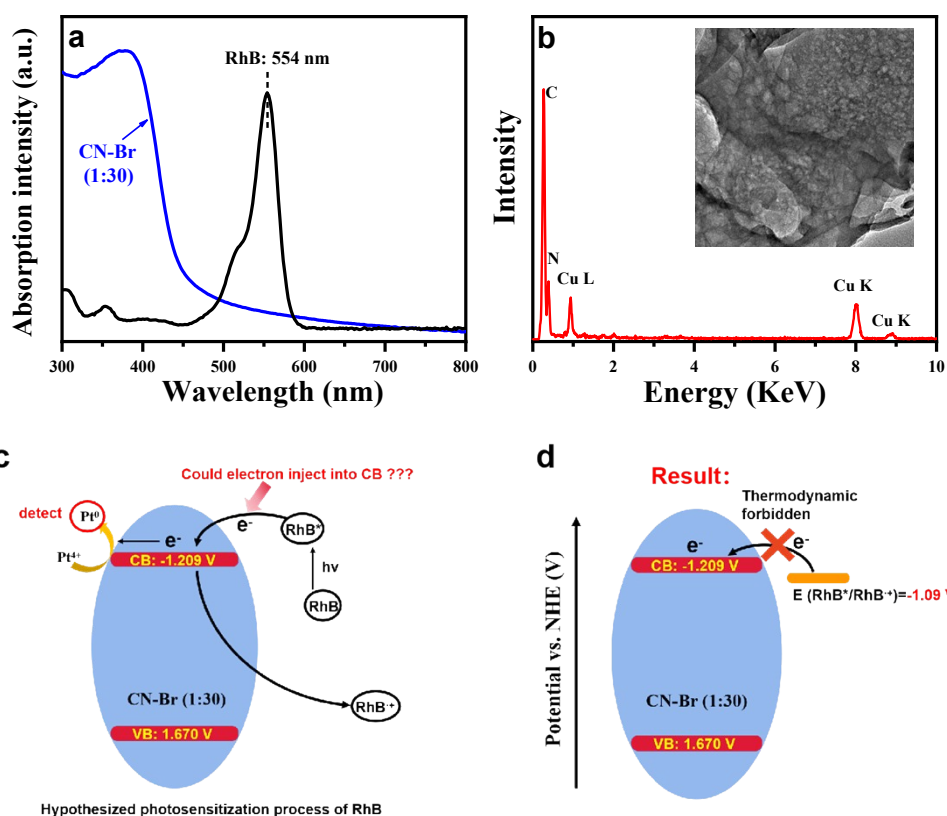


Fig. S10 (a) UV-vis absorbance spectra of RhB solution ($10 \text{ mg}\cdot\text{L}^{-1}$) and CN-Br (1:30) sample. (b) EDS analysis and corresponding TEM image of inset for RhB/CN-Br (1:30) in H_2PtCl_4 aqueous solution after light irradiation with the wavelength of larger 550 nm. (c) Schematic diagram of hypothesized photosensitization process of RhB and (d) actual result.

Analyze the possibility of photosensitization effect. In order to investigate whether visible light photocatalytic activity of RhB degradation is due to the photosensitization effect of dye itself, a series of experiments and characterizations were carried out. As shown the UV-vis absorption spectra of CN-Br and RhB samples in Fig.S10, the absorption band of CN-Br is mainly in the region of 300-450 nm while RhB exhibits an intensive absorption from 450 to 600 nm. According to the above absorption property, light irradiation wavelength is selected to be longer than 550 nm by adding a cut-off

filter of 550 nm. Under the light wavelength of larger 550 nm, it can be speculated that CN-Br is not excited due to inadequate energy and only the chemisorbed RhB is excited to RhB* with active electrons.³ If the degradation mechanism is photosensitization effect of RhB, RhB* should injects the electrons into the CB of CN-Br and these injected electrons could reduced Pt⁴⁺ to Pt⁰. We collected the sample of the above illustration reaction and characterized with TEM images. In Fig. S10, there is no particles assigned to metal Pt⁰ dispersing on the surface of carbon nitride and corresponding EDS analysis only detected C and N elements without any Pt element, which indicates the electron of RhB* is failed to transfer into CN-Br and photosensitization process is not occurred. It is reported that the redox potential of RhB*/RhB⁺ is -1.09 V via photoelectrochemical method.⁴ In our case, the conduction band of CB-Br is determined to be -1.209 V (Fig. 2m-2q), which is more negative than redox potential of RhB*/RhB⁺. Therefore, the electron from excited RhB* is unable to inject to the CB of CN-Br thermodynamically, which further prove the the absence of sensitization effect during RhB degradation.

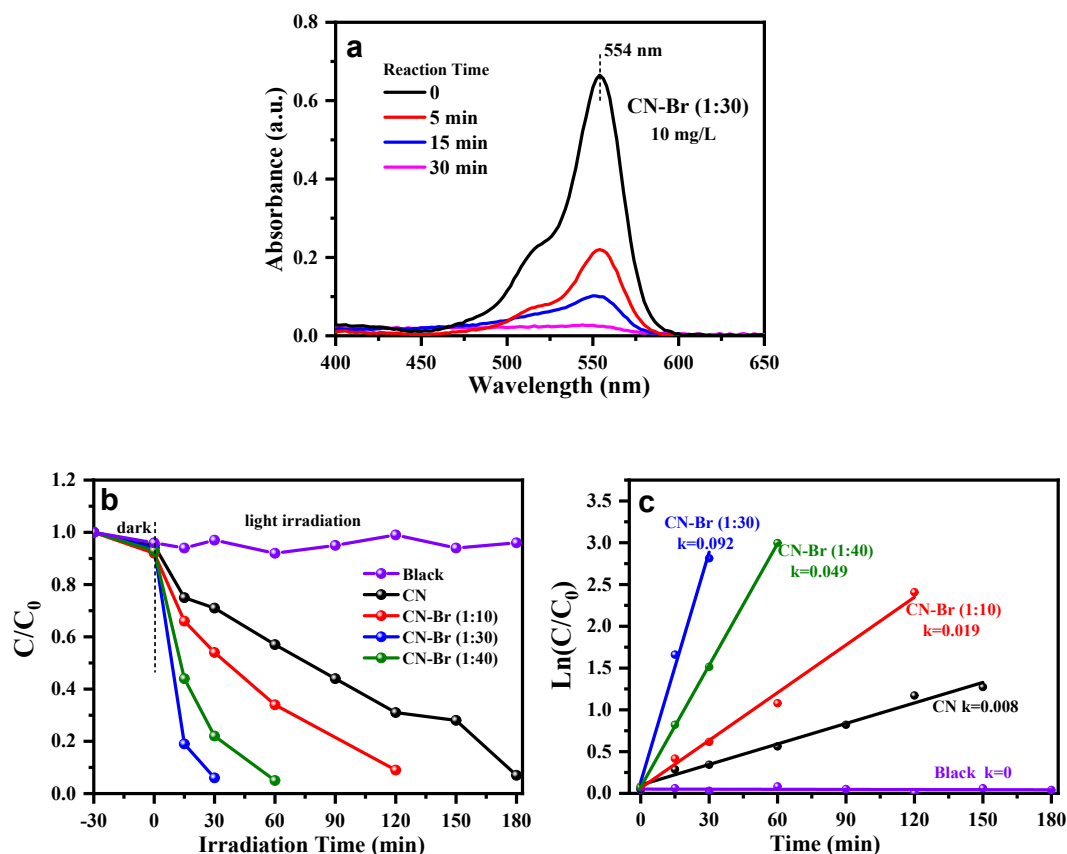


Fig. S11 (a) UV-vis absorbance spectra of RhB solution ($10 \text{ mg}\cdot\text{L}^{-1}$). (b) Photocatalytic performance of bulk CN and CN-Br samples in RhB degradation with visible-light irradiation. (c) The apparent rate constant (k) over bulk CN and CN-Br samples in RhB degradation reaction.

The photocatalytic degradation of rhodamine B (RhB) was carried out in 80 mL $10 \text{ mg}\cdot\text{L}^{-1}$ RhB aqueous solution with 40 mg photocatalyst under visible-light irradiation. The concentration of RhB was monitored by the intensity change of its characteristic absorption peak at 554 nm (Fig. S11a). Before light irradiation, reaction system was kept under dark conditions for 30 min in order to attain an adsorption equilibrium and the RhB concentration shows negligible change in this stage. After 30 min visible-light irradiation, the degradation degree of RhB was 46%, 94%, and 78% for CN-Br (1:10),

CN-Br (1:30), and CN-Br (1:40), respectively. That means CN-Br (1:30) can almost completely degrade RhB within 30 min. Based on pseudo-first-order kinetics degradation, the apparent rate constant (k) was calculated by equation: $k = \ln(C_0/C)/t$ and the result is show in Fig. S11c. Compared with the k of bulk CN (0.008 min^{-1}), CN-Br samples possess much better performance in terms of k values: CN-Br (1:30) (0.092 min^{-1}); CN-Br (1:40) (0.049 min^{-1}); CN-Br (1:10) (0.019 min^{-1}). The CN-Br (1:30) has the highest rate constant of 0.092 min^{-1} , which is almost 11.5 times of that of bulk CN.

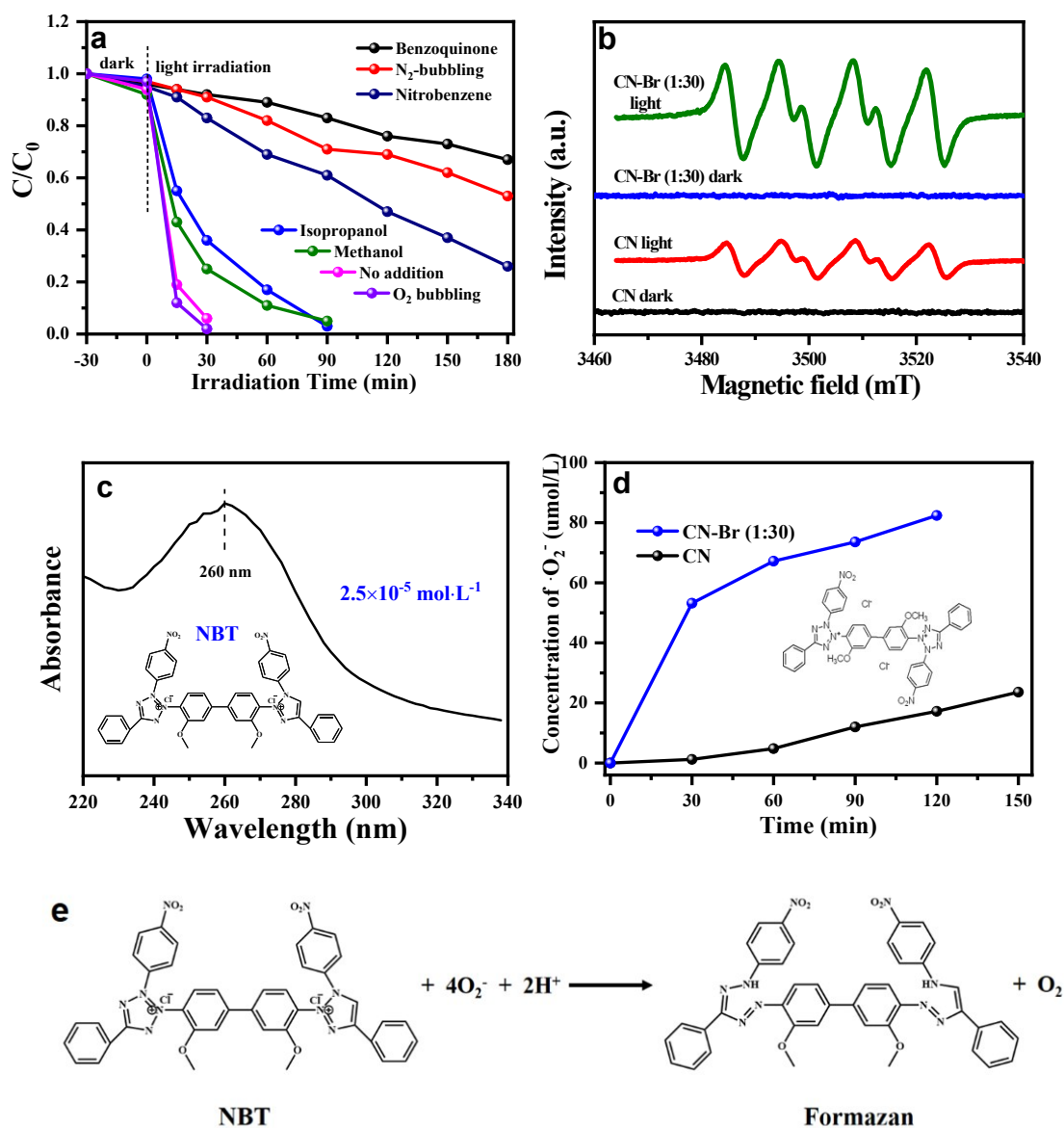


Fig. S12 (a) Effect of quencher additives on the photocatalytic activity of CN-Br (1:30) sample in RhB degradation. (b) EPR spectra of bulk CN and CN-Br (1:30) samples with visible-light irradiation for 300s for the detection of ·O₂⁻ radicals in the presence of DMPO. (c) UV-vis absorbance spectra of NBT solution (2.5 × 10⁻⁵ M). (d) Quantitative determination of ·O₂⁻ generation for bulk CN and CN-Br (1:30) samples via time-dependent degradation of NBT solution (2.5 × 10⁻⁵ M) under visible-light irradiation. (e) Reaction equation between NBT and ·O₂⁻ is 1:4 in molar ratio.

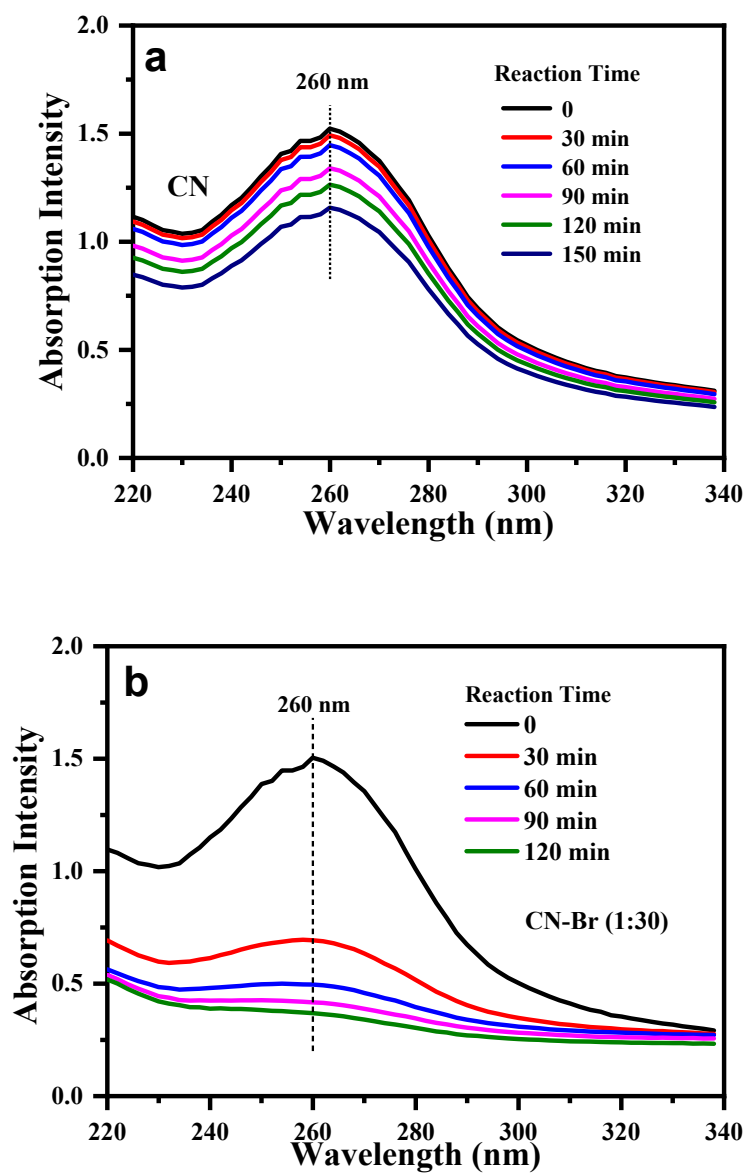


Fig. S13 UV-vis absorbance spectra of degradation NBT reaction upon (a) bulk CN and (b) CN-Br (1:30) sample.

To investigate the main reactive species in the visible-light-driven photocatalytic degradation RhB with CN-Br (1:30) as catalyst, a series of controlled experiments with various gas environment and radical scavengers were implemented. It is found that the degradation efficiency in the inert N₂ atmosphere decrease significantly in comparison with that in air or O₂ atmosphere, proving that the degradation of RhB involves oxygen. Then 1,4-benzoquinone (BQ), nitrobenzene, isopropanol (IPA), and methanol are chosen to act as ·O₂⁻, e⁻, ·OH and h⁺ scavenger, respectively, to identify the intermediate of the RhB degradation.^{5,6} The results are shown in Fig. S12a. It can be seen that the degradation efficiency of RhB dramatically decreases from 94% to 4% in the presence of BQ after 30 min of reaction. When nitrobenzene was added to the reaction system, the degradation efficiency of RhB is also obviously depressed with residual RhB concentration (C₀/C) of 83% after 30 min of reaction. However, the addition of IPA and methanol did not affect the degradation efficiency significantly. These results indicate that superoxide radicals (·O₂⁻) and photogenerated electrons (e⁻) are vital active species in the degradation of RhB instead of ·OH radicals and h⁺. It is generally accepted that ·O₂⁻ radicals, ·OH radicals and h⁺ are main three species for oxidation degradation reaction. But in our case, both ·OH radicals and h⁺ are excluded from our reaction mechanism. The reason is that the valence band (VB) levels of bulk CN and all CN-Br samples are below 1.7 V (Fig. 2q), which are smaller than the oxidation potential of H₂O/·OH (E_{H₂O/·OH} =1.99 V vs. NHE).⁵ The ·O₂⁻ radicals can be formed after O₂ molecule accepting e⁻ due to CB of CN-Br is more negative than the redox potential of (O₂/·O₂⁻ = -0.046 V). In addition, the generated reactive species over

CN and CN-Br under visible light irradiation was studied by spin-trapping electron paramagnetic resonance (EPR) experiment with 5,5-dimethyl-1-pyrroline- N-oxide (DMPO) as a probe, in a (Fig. S12b). No EPR signal was observed for both CN and CN-Br (1:30) samples under dark condition. But under visible light irradiation, both two samples display four resonance signals with an intensity ratio of 1:1:1:1, which is the characteristic EPR signals of DMPO- $\cdot\text{O}_2^-$.⁷ Compared with bulk CN, CN-Br (1:30) presents more enhanced EPR intensity of DMPO- $\cdot\text{O}_2^-$, indicating much better $\cdot\text{O}_2^-$ generation capability for CN-Br than bulk CN. Furthermore, the amount of $\cdot\text{O}_2^-$ generated in the photocatalytic process is also determined by nitroblue tetrazolium (NBT) transformation method.⁸ The characteristic absorption intensity at 260 nm is chosen to quantify the concentration of degradation NBT (Fig. S12c) and the reaction molar ratio between NBT and $\cdot\text{O}_2^-$ is 1:4 (Fig. S12e). As shown in Fig. S11, the $\cdot\text{O}_2^-$ evolution amount of bulk CN and CN-Br (1:30) in the first 30 min are determined to be 1.2 and 53.2 $\mu\text{mol}\cdot\text{L}^{-1}$. This great enhancement of $\cdot\text{O}_2^-$ evolution further demonstrates the high $\cdot\text{O}_2^-$ evolution capability of CN-Br (1:30), which is consistent with the experimental results.

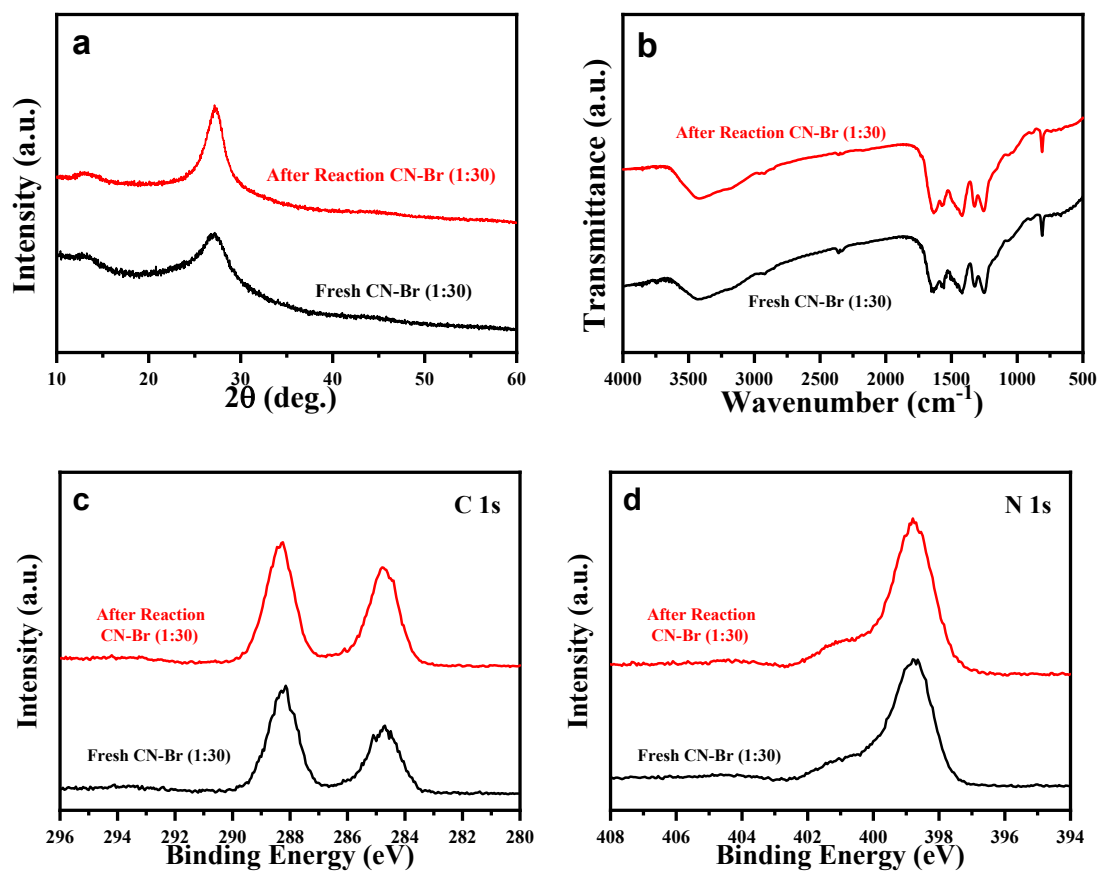


Fig. S14 (a) XRD patterns, (b) FTIR spectra, (c) C 1s and (d) N 1s XPS spectra of CN-Br (1:30) sample before and after reaction.

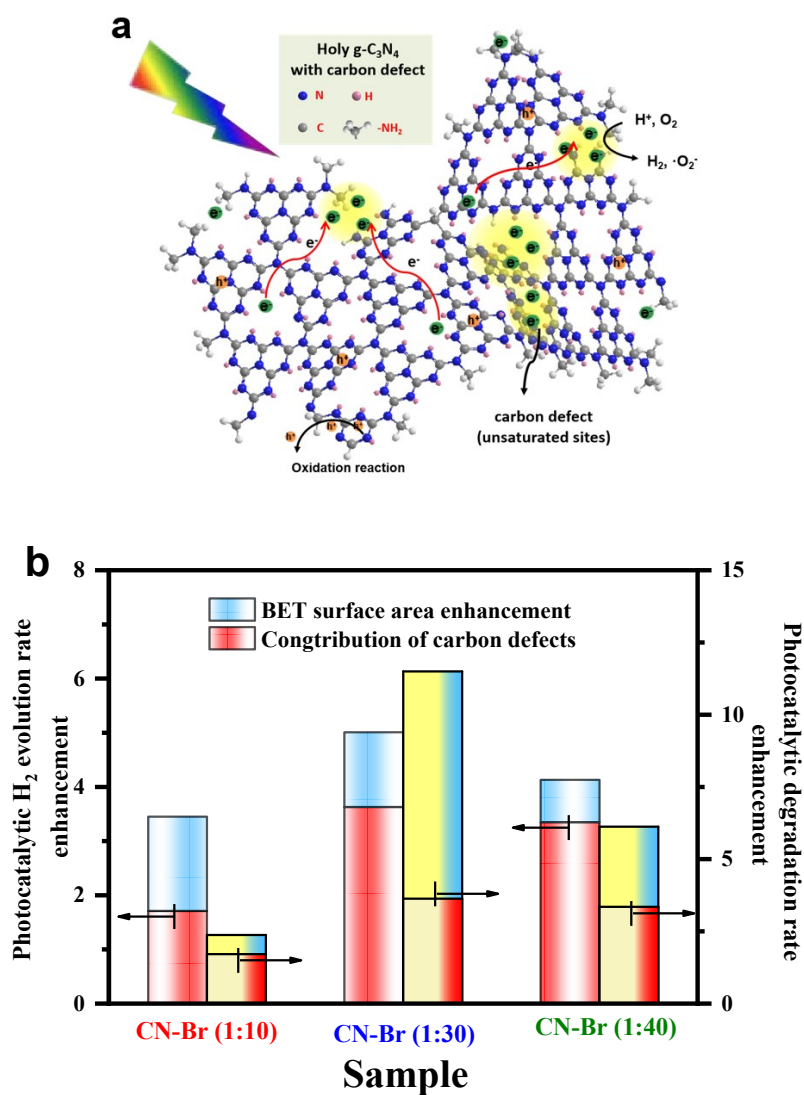


Fig. S15 (a) Illustration of charge behavior in holey $g\text{-C}_3\text{N}_4$ with carbon defect upon light illumination. (b) The enhancement of photocatalytic hydrogen evolution and degradation rate based on BET surface area enhancement and the introduction of carbon defects.

Table S1. The atomic content of C and N elements, and the ratio of C to N of CN and CN-Br samples by using XPS and ICP analysis.

Sample	XPS analysis			ICP analysis		
	C (At%)	N (At%)	C/N Atomic Ratio	C (At%)	N (At%)	C/N Atomic Ratio
CN	44.13	55.87	0.79	44.97	55.03	0.82
CN-Br (1:10)	43.18	56.82	0.76	42.53	57.47	0.74
CN-Br (1:30)	41.52	58.48	0.71	40.71	59.29	0.69
CN-Br (1:40)	39.4	60.6	0.65	38.27	61.73	0.62

Table S2. Composition and chemical properties of CN and CN-Br samples.

Sample	C Atomic content (%)	N Atomic content (%)	C/N Atomic Ratio	C _(N-C=N) percent (%) ^a	The sum of (sp ² _(C-N=C) + sp ³ _{(N-C₃)) to -NH_x ^b}
CN	44.97	55.03	0.82	51.50	10.39
CN-Br (1:30)	40.71	59.29	0.69	40.42	8.60

^a) calculated by peak area of N-C=N to the sum of N-C=N, C-NH_x and graphitic carbon (C-C) in C 1s XPS spectra; ^b) calculated by peak area of the sum of (sp²_(C-N=C) + sp³_(N-C₃)) to -NH_x in N 1s XPS spectra.

Table S3. Normalized degradation efficiency with their BET specific surface areas.

Sample	Apparent rate constant (k)	BET surface area (m²·g⁻¹)	Normalized value of k with BET surface areas (×10⁻⁴ m⁻²·g)[*]
CN	0.008	13.81	5.80
CN-Br (1:10)	0.019	23.56	8.10
CN-Br (1:30)	0.092	50.12	18.4
CN-Br (1:40)	0.049	46.28	10.6

* Normalized value of k was calculated by apparent rate constant (k) divided BET surface area.

References:

1. V. W.-h. Lau, M. B. Mesch, V. Duppel, V. Blum, J. Senker and B. V. Lotsch, *J. Am. Chem. Soc.*, 2015, **137**, 1064-1072.
2. A. Schwarzer, T. Saplinova and E. Kroke, *Coord. Chem. Rev.*, 2013, **257**, 2032-2062.
3. J. Zhao, T. Wu, K. Wu, K. Oikawa, H. Hidaka and N. Serpone, *Environ. Sci. Technol.*, 1998, **32**, 2394-2400.
4. T. Watanabe, T. Takizawa and K. Honda, *J. Phys. Chem.*, 2002, **81**, 1845-1851.
5. Y. Zheng, Z. Yu, H. Ou, A. M. Asiri, Y. Chen and X. Wang, *Adv. Funct. Mater.*, 2018, **28**, 1705407.
6. B. Tian, B. Tian, B. Smith, M. C. Scott, R. Hua, Q. Lei and Y. Tian, *Nat. Commun.*, 2018, **9**, 1397.
7. H. Lan, L. Li, X. An, F. Liu, C. Chen, H. Liu and J. Qu, *Appl. Catal., B*, 2017, **204**, 49-57.
8. S. Zhao, T. Guo, X. Li, T. Xu, B. Yang and X. Zhao, *Appl. Catal., B*, 2018, **224**, 725-732.